Comparative Medicine
Copyright 2018
by the American Association for Laboratory Animal Science

Vol 68, No 2
April 2018
Pages 139–147

Original Research

Brain Iron Distribution after Multiple Doses of Ultra-small Superparamagnetic Iron Oxide Particles in Rats

Andrew W Gorman,[1,*,†] Kofi M Deh,[2,†] Caspar M Schwiedrzik,[3] Julie R White,[4] Ernest Victor Groman,[5] Clark A Fisher,[6] Kelly M Gillen,[2] Pascal Spincemaille,[2] Skye Rasmussen,[7] Martin R Prince,[2] Henning U Voss,[2] Winrich A Freiwald,[6] and Yi Wang[2]

The purpose of this study is to determine the effects of high cumulative doses of ultra-small paramagnetic iron oxide (USPIO) used in neuroimaging studies. We intravenously administered 8 mg/kg of 2 USPIO compounds daily for 4 wk to male Sprague–Dawley rats (Crl:SD). Multiecho gradient-echo MRI, serum iron levels, and histology were performed at the end of dosing and after a 7-d washout period. R2* maps and quantitative susceptibility maps (QSM) were generated from multiecho gradient-echo data. R2* maps and QSM showed iron accumulation in brain ventricles on MR images acquired at the 4- and 5-wk time points. Estimates from QSM data showed ventricular iron concentration was equal to or higher than serum iron concentration. Histologic analysis revealed choroid plexus hemosiderosis and midbrain vacuolation, without iron deposition in brain parenchyma. Serum iron levels increased with administration of both compounds, and a 7-d washout period effectively reduced serum iron levels of one but not both of the compounds. High cumulative doses from multiple, frequent administrations of USPIO can lead to iron deposition in brain ventricles, resulting in persistent signal loss on T2*-weighted images. Techniques such as QSM are helpful in quantifying iron biodistribution in this situation.

Abbreviations: USPIO, ultra-small paramagnetic iron oxide; QSM, quantitative susceptibility mapping; ROI, region of interest; TUNEL, terminal deoxynucleotidyl transferase-mediated dUTP nick-end labeling

Functional neuroimaging capitalizing on MR T2*-weighted imaging is greatly aided by the use of iron-based contrast agents such as ultra-small paramagnetic iron oxide (USPIO) particles. USPIO particles such as monocrystalline iron oxide nanoparticles isolate the cerebral blood flow component of the blood-oxygenation–level-dependent signal and thus provide enhanced sensitivity, reduced large-vessel contribution, improved spatial specificity, and easier interpretation than conventional, blood-oxygenation–level-dependent-based functional MRI.[33] Therefore, they are increasingly being used in preclinical animal[23,58,63] and human[5,70] functional neuroimaging studies. Often, longitudinal studies necessitate multiple small doses of USPIO particles, thus resulting in a large cumulative dose.[5,43,63,70] Repeated dosing in human patients occurs when these compounds are used in the treatment of anemia from iron deficiencies and as drug-delivery vehicles.[68,74] However, information is limited regarding the effects of repeated or high cumulative doses on MR image quality, iron biodistribution, and long-term health effects. Data regarding follow-up pathology is especially sparse. In part, the lack of detailed studies in this area is due to the difficulty of visualizing and quantifying iron biodistribution by using MRI. USPIO nanoparticles are visible as darker regions on T2*-weighted images because they increase the magnetic field inhomogeneity in their vicinity, resulting in an increase in effective relaxation time (that is, T2*) and a consequent signal loss that extends beyond the physical size of the nanoparticle. R2* (that is 1/T2*) mapping is an image processing technique that converts the T2* signal loss into a bright marker for improved visualization and quantification of iron.[14,28,40] Because the T2* signal loss extends beyond the physical size of the USPIO, the R2* value is, in general, not proportional to the USPIO amount. In addition to the effects of iron concentration, R2* depends on other variables that affect relaxation, including contrast agent size, mobility, and magnetic field environment.[9,37,54] Strong T2* effects encountered in high dosing experiments can lead to strong signal losses, making R2* values unreliable.[71] Alternatively, iron can be quantified by using quantitative susceptibility mapping (QSM), an image-processing method that inverts the magnetic field-to-source equation to reconstruct the true magnetic susceptibility distribution in an object from the MR phase images.[16,17,36,47-49,64,72,73] Iron estimation using QSM is highly reproducible;[18,27] independent of environment; free of artifactually increased signal (blooming artifact), resulting in a more accurate representation of size;[21,42] and linear even at high concentrations.

Received: 31 May 2017. Revision requested: 16 Jul 2017. Accepted: 26 Sep 2017.
[1]Institute of Comparative Medicine, Columbia University, New York, New York and Center of Comparative Medicine and Pathology, Memorial Sloan-Kettering Center, Tri Institutional Training Program in Laboratory Animal Medicine and Science, New York, New York ; [2]Joan and Sanford I Weill Medical College, Cornell University, New York, New York; [3]Laboratory of Neural Systems, Rockefeller University, New York, New York, and Neural Circuits and Cognition Lab, European Neuroscience Institute, Gottingen, Germany; [4]Center of Comparative Medicine and Pathology, Memorial Sloan-Kettering Cancer Center, Tri Institutional Training Program in Laboratory Animal Medicine and Science, New York, New York; [5]Skaggs School of Pharmacy and Pharmaceutical Sciences, University of Colorado, Aurora, Colorado; [6]Laboratory of Neural Systems, Rockefeller University, New York, New York; and [7]Comparative Bioscience Center, Rockefeller University, New York, New York
[†]These authors contributed equally to this work
[*]Corresponding author. Email: ag3825@columbia.edu

These features make QSM more suitable than R2* mapping for USPIO quantification in high-dosing experiments.

USPIO compounds consist of an iron oxide core surrounded by a carbohydrate shell that protects the core from contact with blood components.[19] These compounds have been applied as experimental contrast agents to enhance the functional MRI signal[14,28,40,59,63] in the treatment of anemia from iron deficiencies, and as drug-delivery vehicles.[68,74] Core size and coating affect the pharmacologic and biologic properties of USPIO, including clearance rate, iron bioavailability, and activity in vivo.[3,15] In 2009, the US Food and Drug Administration approved the USPIO Feraheme (generic name, ferumoxytol; AMAG Pharmaceuticals, Waltham, MA) for the treatment of iron-deficiency anemia in patients with chronic kidney disease.[50] The recommended dosing for Feraheme is 2 individual 510-mg (about 10 mg/kg) doses administered at least 3 d apart. Toxicity studies, involving a recommended human dose of approximately 37 mg/kg administered daily by intravenous injection for 4 wk to rat and dogs, demonstrated no adverse effects .[9] Dosing for imaging experiments varies with application but can range from 2 to 10 mg/kg in humans,[5,43,65,70] 8 to 10 mg/kg in NHP,[23,40,63] and 1 to 15 mg/kg in rats.[58,76] Repeated administration of USPIO for MRI occurs in MRI-based monitoring of asymptomatic carotid stenosis[69] and in experimental studies where data is acquired longitudinally.[40]

Here, we studied the effects of multiple USPIO administrations (dose, 8mg/kg IV) in rats; this dose is within the range typically reported in imaging experiments[5,23,40,43,58,63,69,70,75] and has a sufficiently long duration to provide insight into the effects of multiple exposures. We studied the effects of 2 commercially available USPIO—ferumoxytol (Feraheme) and Molday ION (BioPhysics Assay Laboratory, Worcester, MA)—to determine whether differences in formulation have biologic effects associated with repeat dosing. Molday ION (30 nm) is similar in size to ferumoxytol (17 to 31 nm) but has a different coating and charge. We noninvasively quantified iron concentration changes over time by using QSM. In addition, we assessed iron accumulation in brain tissue by using histopathology, free iron release from USPIO by using serum analysis, and immune response by performing WBC counts.

Materials and Methods

Study design. Rats were randomly assigned to 1 of 4 treatment groups: group 1 (n = 7), daily administration of ferumoxytol (Feraheme, AMAG Pharmaceuticals) for 4 wk (28 to 31 d); group 2 (n = 7), daily administration of ferumoxytol for 4 wk followed by a 7-d washout period; group 3 (n = 8), daily administration of Molday ION (catalog no. CL-30Q02-7, BioPhysics Assay Laboratory) for 4 wk; and group 4, daily administration of Molday ION for 4 wk followed by a 7-d washout period (n = 6). In each group, 8 mg Fe/kg of USPIO (either ferumoxytol or Molday ION) was administered daily through a jugular catheter. During the 7-d washout period, rats were not given any USPIO treatment. All animals received baseline MRI scans prior to USPIO dosing. Baseline serum iron levels were obtained from blood collected during catheter placement surgery and before the first dose of USPIO was administered. All rats underwent MRI at their respective endpoints and were euthanized through carbon dioxide overdose within 48 h after completion of a follow-up scan. This time window was necessary to accommodate imaging availability times and the ability to process bloodwork in a timely manner. Immediately after euthanasia, whole blood was collected for analyses of serum iron levels, CBC, and serum biochemistry. Individual group size began at 10 rats, but animals whose catheters became nonpatent or dislodged were removed from the study and euthanized.

Animals and procedures. ***Animals.*** Male Sprague–Dawley rats (Crl:SD; n = 28; age, 8 to 10 wk) were obtained from Charles River Laboratories (Worcester, MA). Animals were housed individually in standardized ventilated microisolation cages (115 in^2; Thoren, Hazelton, PA) with corncob bedding (Bed-o-cobs, The Andersons, Maumee, OH) and nesting material (Enviro-dri, Shepherd Specialty Papers, Milford, NJ). Rats had unrestricted access to irradiated rodent laboratory chow (LabDiet 5053, Purina Mills International, St Louis, MO) and acidified municipal tap water. Rats were maintained on a 12:12-h light:dark cycle, with an average ambient room temperature of 22 °C and 30% to 70% relative humidity. Colony health status was monitored quarterly, and animals tested free of the following agents: Sendai virus, pneumonia virus of mice, sialodacyroadenitis–rat coronavirus, rat parvovirus, rat minute virus, Kilham rat virus, Toolan H1 virus, reovirus type 3, lymphocytic choriomeningitis virus, rat theilovirus, rat adenovirus, Hantavirus, cilia-associated respiratory bacillus, *Mycoplasma pulmonis*, *Clostridium piliforme*, *Encephalitozoon cuniculi*, *Salmonella* spp., *Cornynebacterium kutscheri*, *Klebsiella pneumoniae*, *Klebsiella oxytoca*, *Pasteurella pneumotropica*, *Pseudomonas aeruginosa*, *Streptobacillus moniliformis*, *Streptococcus pneumoniae*, β-hemolytic *Streptococcus* spp., pinworms, fur mites, and enteric pathogens. All animal use was approved by the Weill Cornell Medical College IACUC (protocol no. 2014-0053). The animal care and use program at Weill Cornell Medical College is AAALAC-accredited, and all animals are maintained in accordance to the recommendations provided in the *Guide for the Care and Use of Laboratory Animals*.[29]

Surgical procedures. After a 1-wk acclimation period, rats were anesthetized in an isoflurane induction chamber and maintained under isoflurane anesthesia by nosecone. Each rat's eyes were lubricated with ophthalmic ointment. Animals were provided analgesia comprising carprofen (5 mg/kg SC) preoperatively and local infiltration of bupivacaine (5 mg/kg) postoperatively. The ventral neck and intrascapular regions were clipped and prepared for aseptic surgery. A 1.5- to 2.0-cm incision was made in the ventrolateral aspect of the neck, parallel and 0.5 cm lateral to the midline. The left external jugular vein was gently dissected free of surrounding fascia. The cranial aspect of the jugular vein was stabilized and ligated by using 4-0 poliglecaprone suture. Venotomy was performed by using Vannas scissors. A sterilized polyethylene and silicone jugular catheter (Braintree Scientific, Braintree, MA) was inserted to the level of the first retention bead and sutured in place by using 4-0 poliglecaprone suture at the level of the retention bead. Approximately 300 µL whole blood was collected from the catheter for baseline serum iron levels. The catheter was then flushed with 0.2 to 0.3 mL saline and capped by using a small piece of sterilized 50-lb fishing line. When the insertion in the left vein was problematic (4 of 28 catheters placed), an approach to the right external jugular vein was performed. The catheter was tunneled subcutaneously to exit through an approximately 1-cm incision created in the intrascapular region. Catheter patency was assessed by using a 1-mL syringe to aspirate until blood was visible in the catheter. The first dose of USPIO was given at this time, followed by flushing with 0.2 mL saline and 0.2 mL sterile catheter lock solution (heparinized glycerol: 500 IU of heparin in 50% glycerol). The skin incisions were closed by using 3-0 nylon suture. Rats were housed individually postoperatively for the duration of the study, to prevent removal of or damage to the catheter by conspecifics.

MRI data acquisition and postprocessing. All MRI was performed on a 7.0-T scanner (Biospin BioSpec 70/30 USR, Bruker, Billerica, MA) using a custom birdcage coil. T2*-weighted images were acquired with a 3D multiecho gradient-echo sequence with 6 echoes; echo time, 3.2 ms; flip angle, 15°; matrix size, 150 × 150 × 22; voxel size, 0.2 × 0.2 × 1.0 mm^3; and recovery time, 22.5 ms. Rats were anesthetized for MRI by using isoflurane (induction, 3% to 5%; maintenance, 1% to 3%). Complex images were saved in the Digital Imaging and Communications in Medicine format from the MRI scanner and imported into MATLAB (R2012a, The MathWorks, Natick, MA) for postprocessing. All echoes from the Digital Imaging and Communications in Medicine images were combined into a complex MATLAB data structure for convenient processing into 3 types of images. Magnitude images were generated by taking the sum of squares of the absolute of the complex data structure.[61] R2* images were generated from the absolute value of the complex data by using a fast monoexponential Auto Regression on Linear Operations fitting algorithm.[56] A voxel-wise nonlinear fit of the multiecho complex data was performed to produce a field map, which was unwrapped by using a graph-cut algorithm.[20,49] A binary mask was generated for QSM reconstruction by digitally stripping the skull from the rat's head on the magnitude image by using the Brain Extraction Tool software[31] and binarizing the skull-free brain data by using a selected threshold of the pixel value. This step usually improves the quality of the QSM map by restricting the range of susceptibility values that are reconstructed.[72] The QSM map was then constructed by total field inversion of the unwrapped field, with the preconditioner set to 1 for voxels inside the mask and 1000 for voxels outside the mask, a regularization (λ) value of 1000, and iteratively regularized least-squares error correction. An outline of the procedure is shown in Figure 1 A.

Quantitative imaging analysis. Regions of interest (ROI) were prescribed on the central slice of the magnitude image by using the Waxholm Space rat brain atlas as a guide.[55] The brain regions analyzed were the corpus callosum, striatum, thalamus, hypothalamus, cortex, and ventricles. Mean QSM voxel values for ROI drawn on 3 brain slices in these regions were recorded (Figure 1 B). Susceptibility values of CSF measured in the ventricles are typically used as convenient references for other regions of the brain for QSM quantification,[18,44,45] but this approach was not possible because of considerable enhancement of the ventricles after contrast injection. However, we noted that the susceptibility values measured in the hypothalamus region showed the least standard deviation (Figure 1 B). This observation is consistent with the limited vascularity of the thalamic region of the rat brain and provides justification for the use of the hypothalamus as the reference region. The mean ROI values, referenced to the hypothalamus, were converted to contrast agent concentration by division with the molar susceptibility of ferumoxytol and Molday ION, which were determined from a phantom calibration to be 440 ± 32 ppm L/mol and 1013 ± 36 ppm L/mol, respectively.

Hematology and serum chemistry, including serum iron levels. Baseline iron serum levels were assessed by using whole blood collected via syringe through the jugular catheter and aliquoted into a serum separator and EDTA blood collection tubes. CBC and serum chemistry analyses were performed (Laboratory of Comparative Pathology, Center for Comparative Medicine, Memorial Sloan Kettering Cancer Center). Serum iron levels were measured by using a colorimetric assay. After chronic USPIO administration followed by CO_2 inhalation euthanasia, whole blood was collected by cardiocentesis into a serum separator and EDTA blood collection tubes. Serum biochemistry, CBC, and serum iron levels were assessed by the same methods as for the baseline analysis. Hematology and chemistry results were evaluated by using reference values of male CRL:CD(SD).[25]

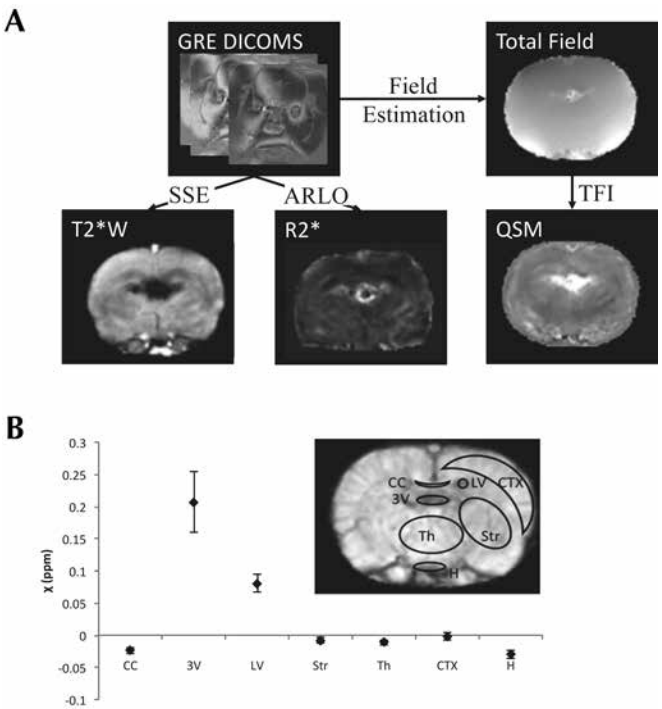

Figure 1. (A) An outline of the postprocessing steps for generating quantitative images from gradient-echo (GRE) Digital Imaging and Communications in Medicine images (DIACOMS) by using autoregression on linear operations (ARLO) fast monoexponential fitting for R2* maps and total field inversion (TFI) for QSM maps. T2*-weighted (T2*W) images were generated by using sum-of-squares estimation. (B) Mean values and standard deviations of mean susceptibility values from ROI in selected regions of the rat brain. Sample ROI are shown on the inset image. The brain regions analyzed were the corpus callosum (CC), third ventricle (3V), left ventricle (LV), striatum (Str), thalamus (Th), neocortex (CTX), and hypothalamus (H).

Necropsy and histopathology. A complete gross necropsy was performed without fixative perfusion on all rats immediately after euthanasia. The brain, liver, and spleen were fixed in 10% buffered formalin. Representative sections of the brain, liver, and spleen were embedded in paraffin, sectioned at 5 µm, and stained with hematoxylin and eosin. A board certified veterinary pathologist evaluated all tissue sections. Four coronal sections of the brain were evaluated, to include all areas from the forebrain to the brainstem, paying particular attention to areas that corresponded to ROI on MRI. Standard sections of all other tissues were evaluated for the presence and severity of iron accumulation (hemosiderosis) and for cellular damage resulting from iron accumulation (hemochromatosis). Staining with Prussian blue was done on brain tissues of all groups and liver and spleen of some animals at the discretion of the veterinary pathologist, to confirm the presence of iron. Tissue hemosiderosis severity for each treatment group was determined according to the quantity of iron-containing cells. Tissues assessed by the veterinary pathologist were subjectively ranked on a score of 0 to 4, according to the intensity of uptake of Prussian blue stain: 0, no uptake; 1, minimal uptake; 2, mild; 3, moderate; and 4, severe tissue hemosiderosis. Sections were also evaluated for inflammation, degenerative changes, and any other noteworthy lesions. When tissue vacuolation was observed, activated caspase 3 (Cleaved caspase 3 [Asp175] Antibody, catalog no. 9661, Cell Signaling, Danvers, MA) and terminal deoxynucleotidyl

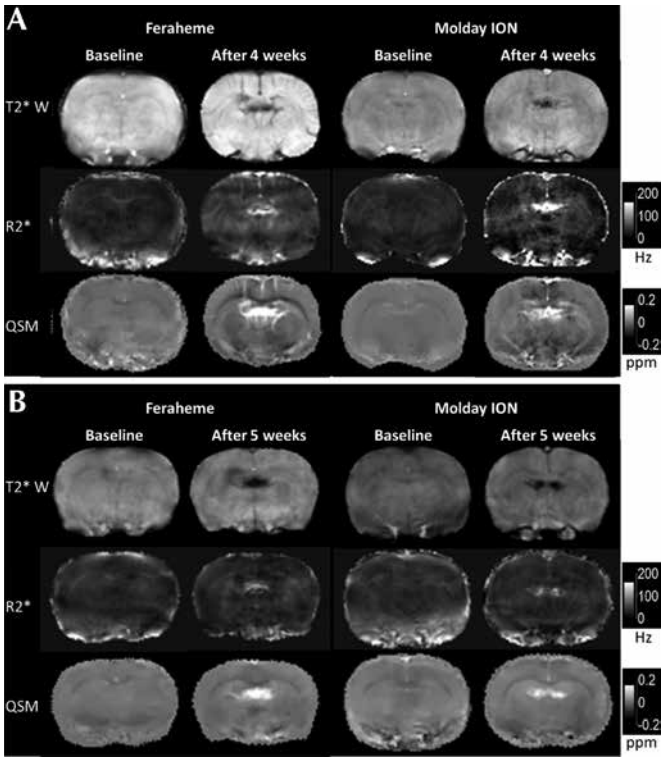

Figure 2. Magnitude, R2*, and QSM images from MRI gradient-echo imaging of rat brains before and after (A) 4 wk of daily injections and (B) 4 wk of daily injections and 1 wk without injections. Each image was postprocessed from all echoes of the gradient-echo acquisition as described in the Methods section. Contrast enhancement with repeated dosing of ferumoxytol and Molday ION was primarily localized to the ventricles.

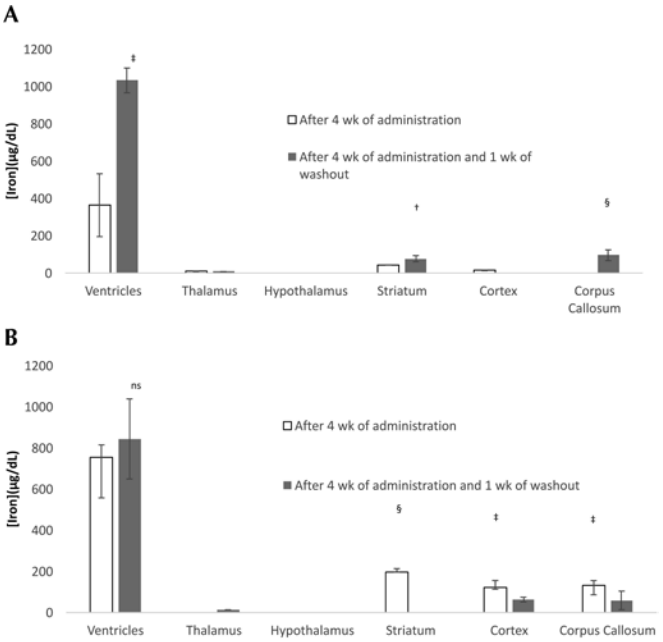

Figure 3. Iron concentration (mean ± SEM [error bars]) over all rats estimated by using QSM values for selected brain regions in rats receiving (A) ferumoxytol or (B) Molday ION. Iron concentrations are calculated from the difference between the QSM values at baseline and endpoint, relative to the hypothalamus. Thus, the USPIO concentration at baseline is assumed to be 0. Significant differences (Student *t* test) are indicated as *, $P < 0.05$; †, $P < 0.01$; and ‡, $P < 0.001$.

transferase-mediated dUTP nick-end labeling (TUNEL) staining[12,24] were done on select brain sections to confirm true degenerative changes and rule out tissue processing artifacts.

Data analysis. Comparison of discrete variables of choroid plexus hemosiderosis and midbrain vacuolation between ferumoxytol and Molday ION study groups were evaluated by using χ^2 analyses. Continuous variables were evaluated by using ANOVA with Bonferonni posthoc analyses for all differences that achieved statistical significance (that is, $P < 0.05$). One-sample *t* tests were used to compare mean WBC, ALT, and AST values for the overall study population and all study groups against reference values. Two-way repeated-measures ANOVA was used to evaluate between-group differences in iron concentration of the corpus callosum, third ventricle, lateral ventricle, caudate putamen, thalamus, neocortex, and globus pallidus from baseline to 4 wk. All analyses were performed by using SPSS version 22.0 (IBM, Armonk, NY). Rats removed from study due to catheter nonpatency or loss were not included in data analysis.

Results

Animals and procedures. Individual group size began at $n = 10$, but rats whose catheters became nonpatent or dislodged were removed from the study and euthanized. In addition, 3 animals (10% of study population) had mild facial edema postoperatively, which resolved spontaneously within 48 h after surgery.

Quantitative MRI. Representative axial views of the brains of rats injected with ferumoxytol and Molday ION are shown in Figure 2. Each column shows the magnitude, R2*, and QSM images for the central slice of the MRI image at baseline and after 4 wk of daily USPIO injections without and with 1 wk of washout. Contrast enhancement with repeated dosing was primarily localized to the ventricles and exhibited large variability between different rats. The USPIO concentration estimates for each brain region averaged over all rats in each group are shown in Figure 3. The largest changes in USPIO concentration after 4 wk of USPIO administration occurred in the ventricles. At 1 wk after the last dose, estimates of USPIO concentration in the ventricles showed a significant increase for rats ($P = 0.0002$) that received ferumoxytol and a nonsignificant increase ($P = 0.71$) for rats that received Molday ION. Estimates of USPIO concentrations for ROI in brain regions appeared to show a slight increase in the striatum and corpus callosum for rats receiving ferumoxytol and a decrease in the same regions for rats receiving Molday ION after 1 wk of washout (Figure 3).

Necropsy and histopathology. No abnormalities were noted during gross necropsy. Prussian blue staining of the brain revealed variable iron deposition only within the choroid plexus (Figure 4 A and B). Rats that received 4 wk of ferumoxytol were negative for hemosiderin within the choroid plexus, those given 4 wk ferumoxytol followed by 1 wk of washout had a mean score of 0.43 (range, 0 to 1), animals administered 4 wk of Molday ION had a mean score of 0.62 (range, 0 to 2), and those that had 4 wk of Molday ION and a 1-wk washout had a mean score of 0.66 (range, 0 to 2; $P = 0.176$). All groups demonstrated subjectively severe (score, 4) hemosiderosis of the liver and spleen (Figure 4 C and D) without associated degenerative changes. Hemosiderin, identified by Prussian blue staining, was present in macrophages in the splenic white and red pulp and in hepatic Kupffer cells. In addition, the unexpected pathologic tissue change of midbrain parenchyma vacuolation (Figure 4 E and F) was ranked according to severity by using a scale of 0 (no change) to 4 (severe vacuolation), yielding a score of 2 for all

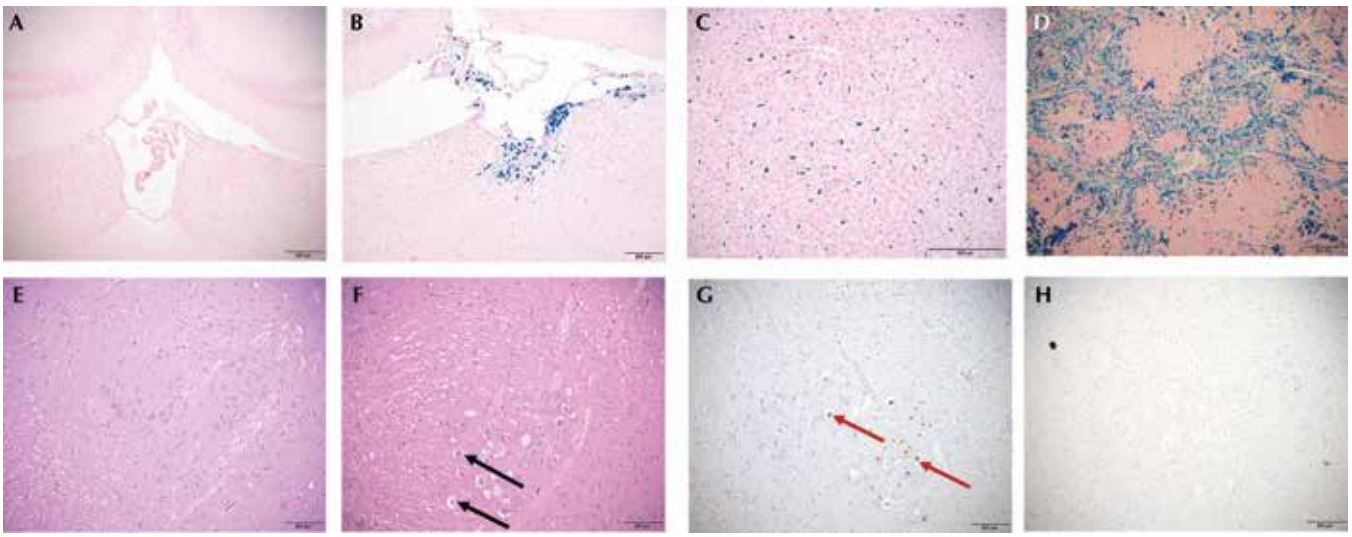

Figure 4. Choroid plexus from (A) a rat with a hemosiderosis score of 0 (no iron accumulation) and (B) a rat with a hemosiderosis score of 2 (moderate iron accumulation). (C) Liver and (D) spleen also showed iron accumulation. Prussian blue staining. Midbrain from (E) a rat with a vacuolation score of 0 (no vacuolation) and (F) a rat with a vacuolation score of 2 (moderate vacuolation). Midbrain of a rat with a vacuolation stained with (G) TUNEL and (H) caspase. Black arrows indicate vacuolation; red arrows indicate TUNEL-positive cells. TUNEL-positive staining suggests that vacuolation is not a processing artifact, and caspase-negative staining suggests that these cells are undergoing apoptosis. All rats depicted in the photomicrographs received Molday ION, but the findings are representative of the scoring systems used to evaluate all experimental groups. Scale bars, 200 µm.

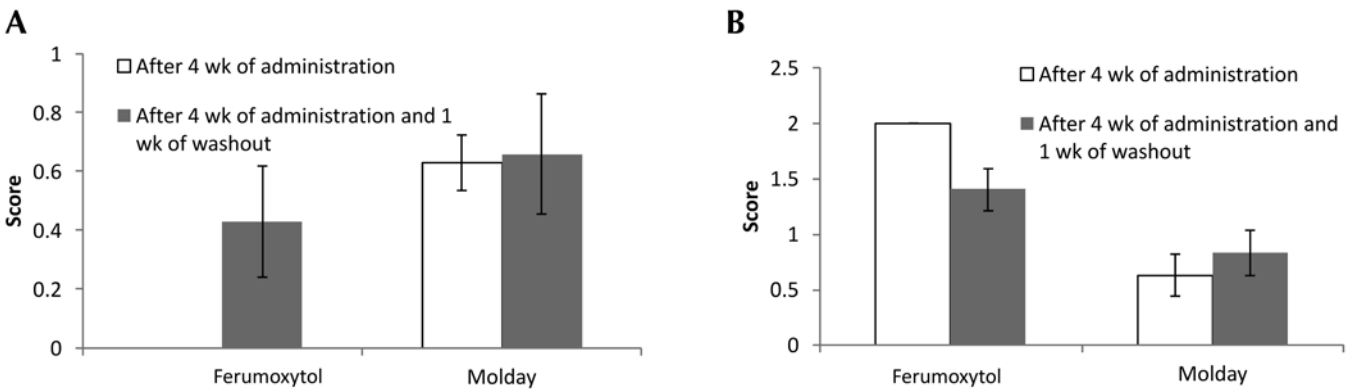

Figure 5. Scores (mean ± SEM [error bars]) for (A) choroid plexus hemosiderosis and (B) midbrain vacuolation after 4 wk of dosing without and with 1 wk of washout are shown for rats that received ferumoxytol and Molday ION.

animals that received 4 wk of ferumoxytol and mean scores of 1.4 for those given 4 wk ferumoxytol followed by 1 wk of washout, 0.63 for rats administered 4 wk of Molday ION, and 0.83 for that had 4 wk of Molday ION and a 1-wk washout, with a range of 0 to 2 for all animals ($P = 0.008$; Figure 5). Vacuolation was noted on sections stained with hematoxylin and eosin. The positive TUNEL staining in these sections suggests that vacuolation is the result of degenerative changes and rules out vacuolation as a tissue-processing artifact.

Hematology and serum chemistry, including serum iron levels. All rats exhibited significant increases in serum iron from baseline to endpoint (Figure 6). When compared with ferumoxytol, Molday ION yielded a larger serum iron increase ($P = 0.001$). Postdosing serum iron levels were lower in the Molday ION group with washout than without washout ($P = 0.01$). No animals exhibited adverse clinical effects during the USPIO dosing or washout period.

Hematology showed elevated WBC counts in some rats and a significant ($P = 0.036$) increase in the WBC counts of the ferumoxytol groups when compared with the Molday ION groups. WBC counts did not differ between groups with or without washout ($P = 0.150$). Serum chemistry values showed that some animals in all groups had elevated ALT and AST values, although no significant differences emerged when ferumoxytol was compared with Molday ION ($P = 0.311$ and $P = 0.668$ respectively) when washout was not considered. In rats given Molday ION, ALT showed an increase from 129.6 without washout to 741.3 after washout ($P = 0.017$).

Discussion

The results of this study show that rats receiving daily, intravenous USPIO injections exhibit signal changes within the brain ventricles on MRI. Estimates of iron concentration in the CSF by using QSM were as high (for Molday ION) or higher (ferumoxytol) than that in serum. A 7-d washout period did not reduce the USPIO content in brain ventricles on MR images. An unexpected finding of this study was that repeated dosing of USPIO resulted in degenerative midbrain vacuolation similar to observations reported in mice lacking iron regulatory protein (IRP2), which regulates the transcription of transferrin and ferritin.[26]

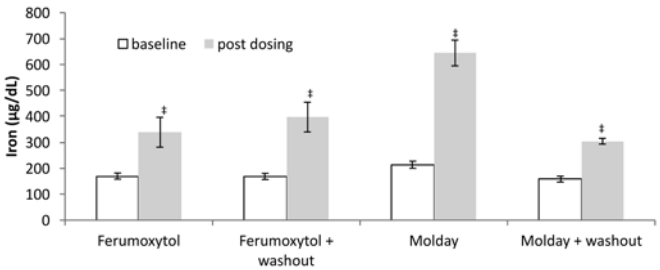

Figure 6. Serum iron levels (mean ± SEM [error bars]) showed significant increases for each group after 4 wk of dosing. Serum iron was significantly higher for rats given Molday ION compared with ferumoxytol. Serum iron in rats given Molday ION was significantly lower without washout than with a 1-wk washout. Significant differences (Student *t* test) are indicated as *, $P < 0.05$; †, $P < 0.01$; ‡, $P < 0.001$; and §, $P < 0.0001$.

Increased total iron content of the brain has been reported after iron nanoparticle injection, but those studies did not perform MRI quantification to obtain brain iron biodistribution.[30,32] The results of our study demonstrate strong and persistent localization of iron to the choroid plexus and ventricles. The exact mechanism by which iron from USPIO is incorporated into the choroid plexus and CSF has yet to be identified. Previous studies have established that USPIO are taken up by brain macrophages, particularly perivascular and choroid plexus macrophages.[35,62] Our study confirms liver and spleen as major sites for the deposition of USPIO;[39] excess USPIO are known to accumulate in other macrophage-rich organs, including the lungs and fatty tissue, especially when injected in high doses.[41] Although we did not test for macrophages in the CSF, reports of macrophage trafficking through the choroid plexus suggest that they may be a route of iron entry into the CSF.[51] In addition, free iron is released from USPIO inside macrophage vesicles for storage in ferritin or transfer to the plasma.[3,4,15] Free iron in the plasma is bound by transferrin to form a complex that is taken up by receptor-mediated endocytosis into capillary-lining endothelial cells at the blood–brain barrier. The iron–transferrin complex is exported from the endothelial cell into the brain's CSF, where it is subsequently exported into the lateral ventricles through the choroid plexus. CSF flows from the lateral ventricles into the third ventricle, continuing along the cerebral aqueduct and the fourth ventricle, eventually emptying into the subarachnoid space.[60] Consequently, iron is transported to all ventricles, resulting in MRI signal changes in the brain ventricles. How iron is reabsorbed from the ventricular fluid back into the plasma is still subject to speculation, although the process is believed to occur through the arachnoid villi that protrude into the venous sinuses.[11,60] The failure of a 1-wk clearance period to significantly reduce CSF iron levels in the current study indicates incomplete elimination in this model after a maximum of 1 wk of washout and suggests that the mechanism for brain iron elimination may be similar to that previously reported for manganese: a receptor-mediated expulsion from the brain into CSF, followed by diffusion-mediated reentry from the CSF back into the plasma.[76] Although ROI analysis appeared to reveal slight changes in iron content in the striatum and corpus callosum, these changes may be attributed to changes within the cerebral blood vessels rather than to deposition of iron in the brain parenchyma, because histology revealed no such deposition.

The different patterns of serum iron accumulation exhibited by the 2 USPIO formulations may be understood by comparing their half-lives. Because both compounds have similar size, the difference in their half-lives depends primarily on the difference in surface charges because of their respective coating. More positively charged surface coatings are expected to bind more readily to negatively charged serum components, forming large aggregates, which are rapidly cleared by the mononuclear phagocyte system, thus resulting in a shorter half-life.[6,46] By design, ferumoxytol has a strongly negative surface coating to minimize binding to serum components, for maximal accumulation in the liver. Conversely, Molday ION is coated with a weakly negative reduced dextran coating for extended blood half-life and increased accumulation in the lymph nodes. The reported half-life for ferumoxytol in rats is 67 min,[65] whereas that of dextran-coated Ferumoxtran 10 (also known as Sinerem and Combidex; AMAG Pharmaceuticals), which is similar to Molday ION, is about 150 min.[8] However, increased concentration and repeated dosing can have effects on apparent half-life, because the normal clearance mechanisms may be overloaded and therefore do not reflect the half-life when nanoparticle concentration is limiting. During dosing, serum iron continued to increase for both ferumoxytol and Molday ION groups. However, the shorter half-life of ferumoxytol likely allows for more rapid iron clearance once dosing is discontinued, thus supporting the decrease in serum iron after a washout period in ferumoxytol-treated rats, whereas the decrease was nonsignificant in the Molday ION group.

Histopathology after chronic dosing with and without washout revealed iron accumulation only in the choroid plexus. This finding is consistent with the fact that neurons generally lack ferritin, the iron-storage protein.[52] Midbrain vacuolation was identified histologically, and necrosis was confirmed by TUNEL immunohistochemistry. Midbrain vacuolation, which serves as an early sign of cell death, does not occur spontaneously in normal rats of the age used in these experiments. Because mechanisms for iron uptake into neurons and astrocytes exist,[11,13] an intriguing possibility is that vacuole formation in the midbrain of rats may be linked to increased uptake of iron by neuronal bodies, leading to cell damage through oxidative stress from reactive oxygen species created by the Fenton reaction, which is catalyzed by ferrous iron released from USPIO.[26,57,66] Specifically designed long-term iron-dosing studies are necessary to further investigate the possibility that free iron from USPIO administration contributes to the production of highly reactive hydroxyl radicals and thus promotes cell death.

Rats in the ferumoxytol groups showed elevated WBC counts compared with those in the Molday ION groups. WBC patterns were consistent with a stress leukogram of lymphopenia and monocytosis. They also are consistent with reports of increases in WBC count when animals are exposed to USPIO by inhalation,[38] an effect that has been interpreted as due to the immune's system effort to eliminate USPIO through circulating WBC such as monocytes.[3] The washout period did not have a significant effect on reducing WBC counts in either the ferumoxytol or Molday ION groups and suggests a longer washout period is required for return to normal WBC count. ALT and AST were elevated in several animals in all groups, with a significant increase in ALT in the Molday ION group without washout compared with washout. Although these findings are usually indicative of liver pathology, no pathologic changes were seen on hepatic histopathology. The only change noted on histology of the liver was hemosiderosis confirmed with Prussian blue staining, which was not accompanied by tissue pathology. The elevation in liver enzymes may be indicative of early hepatic pathology or subclinical elevation. Measuring organ weights should be considered for future studies, but weight may not be an accurate way to assess iron accumulation in the spleen, for

which weight can vary widely due to the presence of lymphoid hyperplasia and extramedullary hyperplasia. Future studies could consider measuring tissue iron directly or by electron microscopy. Although hemosiderin can be found in the spleen of aged rats as a result of extramedullary hematopoiesis, the veterinary pathologist deemed the levels found as a result of USPIO administration to be well beyond what is typically seen in rats.[2]

All groups started with 10 rats each, but several animals from each group were unable to complete the study due to loss of catheter or catheter patency. Although we anticipated some attrition, the use of an absorbable suture material may have contributed to the larger-than-expected values. Poliglecaprone suture has an absorbable half-life of 7 to 14 d, with a rapid loss of tensile strength. We recommend using a nonabsorbable suture in future studies.

More generally, the results obtained in our current study suggest that patients receiving frequent USPIO injections for repeated imaging or blood or iron transfusions should be monitored by using a contrast technique such as QSM or susceptibility-weighted imaging. Two radiologic notes have reported darkening of the choroid plexus on T2*- and susceptibility-weighted images of patients receiving transfusions.[22] The first involved a 7-y-old boy with Diamond–Blackfan anemia who was transfusion-dependent by the age of 4. Laboratory studies showed excessively high blood iron levels and decreased signal intensity on the choroid plexus on T2-weighted MRI.[34] Similar results were obtained from a 16-y-old woman, who exhibited the additional symptoms of a headache, dizziness, and numbness in the arms.[67] In studies where USPIO compounds are given repeatedly, concurrent administration of an iron chelation agent should be considered, in efforts to reduce serum iron levels and potential for tissue accumulation. An FDA-approved iron chelator, deferiprone, has been shown to effectively chelate iron in the brain associated with Friderich ataxia.[1] In contrast to iron-chelation agents that target hepatic and splenic iron stores, deferiprone can reduce brain iron accumulation without interfering with normal brain iron signaling.[7,53] Additional studies, which include control animals, to assess the efficacy and safety of chelation agents in preventing or eliminating iron accumulation in the brain as a result of chronic USPIO administration are warranted.

Acknowledgments

This study was funded in part through the NIH/NCI Cancer Center Support Grant P30-CA008748. KD is supported by NIH grants RO1 EB013443, RO1 NS090464, and 1F31EB019883. CMS was supported by a Human Frontier Science Program Long-Term Fellowship (LT001118/2012-L) and is currently funded by the European Union's Horizon 2020 Research and Innovation Programme under the Marie Skłodowska-Curie grant agreement number 706519. CAF was supported by NIH MSTP grant GM007739. This research was supported by The New York Stem Cell Foundation grant NYSCF-R-NI23. WAF is a New York Stem Cell Foundation-Robertson Investigator. The funders had no role in study design, data collection, and analysis, decision to publish, or preparation of the manuscript.

References

1. **Abbruzzese G, Cossu G, Balocco M, Marchese R, Murgia D, Melis M, Galanello R, Barella S, Matta G, Ruffinengo U, Bonuccelli U, Forni GL.** 2011. A pilot trial of deferiprone for neurodegeneration with brain iron accumulation. Haematologica **96:**1708–1711.
2. **Anver MR, Cohen BJ, Lattuada CP, Foster SJ.** 1982. Age-associated lesions in barrier-reared male Sprague–Dawley rats: a comparison between Hap:(SD) and Crl:COBS[R]CD[R](SD) stocks. Exp Aging Res **8:**3–24.
3. **Arami H, Khandhar A, Liggitt D, Krishnan KM.** 2015. In vivo delivery, pharmacokinetics, biodistribution, and toxicity of iron oxide nanoparticles. Chem Soc Rev **44:**8576–8607.
4. **Balakrishnan VS, Rao M, Kausz AT, Brenner L, Pereira BJ, Frigo TB, Lewis JM.** 2009. Physicochemical properties of ferumoxytol, a new intravenous iron preparation. Eur J Clin Invest **39:**489–496.
5. **Baumgartner R, Cho W, Coimbra A, Chen C, Wang Z, Struyk A, Venketasubramanian N, Low M, Gargano C, Zhao F, Williams D, Reese T, Seah S, Feng D, Apreleva S, Petersen E, Evelhoch JL.** 2017. Evaluation of an fMRI USPIO-based assay in healthy human volunteers. J Magn Reson Imaging **46:**124–133.
6. **Blank F, von Garnier C, Gehr P, Rothen-Rutishauser B.** 2014**.** Translocation across the air–blood tissue barrier, p 169–182. In: Tsuda A, Gehr P editors. Nanoparticles in the lung: environmental exposure and drug delivery. CRC Press.
7. **Boddaert N, Le Quan Sang KH, Rötig A, Leroy-Willig A, Gallet S, Brunelle F, Sidi D, Thalabard JC, Munnich A, Cabantchik ZI.** 2007. Selective iron chelation in Friedreich ataxia: biologic and clinical implications. Blood **110:**401–408.
8. **Bonnemain B**. 1998. Pharmacokinetic and hemodynamic safety of 2 superparamagnetic agents, Endorem and Sinerem, in cirrhotic rats. Acad Radiol **5 Suppl 1**:S151–S153; discussion S156.
9. **Bourrinet P, Bengele HH, Bonnemain B. Dencausse A, Idee JM, Jacobs PM, Lewis JM.** 2006. Preclinical safety and pharmacokintetic profile of feuromoxatrn-10, an ultrasmall superparamagnetic iron oxide magnetic resonance contrast agent. Invest Radiol **41:**313–324.
10. **Bowen CV, Zhang X, Saab G, Gareau PJ, Rutt BK.** 2002. Application of the static dephasing regime theory to superparamagnetic iron-oxide loaded cells. Magn Reson Med **48:**52–61.
11. **Bradbury MW.** 1997. Transport of iron in the blood–brain–cerebrospinal fluid system. J Neurochem **69:**443–454.
12. **Cell Signaling Technology.** [Internet]. 2017. SignalStain apoptosis (cleaved caspase-3) IHC detection kit 12692. Available at: https://www.cellsignal.com/products/primary-antibodies/apoptosis-cleaved-caspase-3-ihc-detection-kit/12692.
13. **Codazzi F, Pelizzoni I, Zacchetti D, Grohovaz F.** 2015. Iron entry in neurons and astrocytes: a link with synaptic activity. Front Mol Neurosci **8:**1–6.
14. **D'Arceuil H, Coimbra A, Triano P, Dougherty M, Mello J, Moseley M, Glover G, Lansberg M, Blankenberg F.** 2013. Ferumoxytol enhanced resting state fMRI and relative cerebral blood volume mapping in normal human brain. Neuroimage **83:**200–209.
15. **Danielson BG.** 2004. Structure, chemistry, and pharmacokinetics of intravenous iron agents. J Am Soc Nephrol **15 Suppl 2:**S93–S98.
16. **de Rochefort L, Brown R, Prince MR, Wang Y.** 2008. Quantitative MR susceptibility mapping using piece-wise constant regularized inversion of the magnetic field. Magn Reson Med **60:**1003–1009.
17. **de Rochefort L, Liu T, Kressler B, Liu J, Spincemaille P, Lebon V, Wu J, Wang Y.** 2010. Quantitative susceptibility map reconstruction from MR phase data using Bayesian regularization: validation and application to brain imaging. Magn Reson Med **63:**194–206.
18. **Deh K, Nguyen TD, Eskreis-Winkler S, Prince MR, Spincemaille P, Gauthier S, Kovanlikaya I, Zhang Y, Wang Y.** 2015. Reproducibility of quantitative susceptibility mapping in the brain at 2 field strengths from 2 vendors. J Magn Reson Imaging **42:**1592–1600.
19. **Di Marco M, Sadun C, Port M, Guilbert I, Couvreur P, Dubernet C.** 2007. Physicochemical characterization of ultrasmall superparamagnetic iron oxide particles (USPIO) for biomedical application as MRI con st agents. Int J Nanomedicine **2:**609–622.
20. **Dong J, Liu T, Chen F, Zhou D, Dimov A, Raj A, Cheng Q, Spincemaille P, Wang Y.** 2015. Simultaneous phase unwrapping and removal of chemical shift (SPURS) using graph cuts: application in quantitative susceptibility mapping. IEEE Trans Med Imaging **34:**531–540.
21. **Eskreis-Winkler S, Deh K, Gupta A, Liu T, Wisnieff C, Jin M, Gauthier SA, Wang Y, Spincemaille P.** 2014. Multiple sclerosis lesion geometry in quantitative susceptibility mapping (QSM) and phase imaging. J Magn Reson Imaging **42:**224–229.
22. **Fernández Viñas M, Sánchez-Montañez A, Salazar J, Ng Wong YK, Sánchez AL, Gaete J, Adrián Lozano L, Delgado I, Vazquez E.** 2015. Pediatric choroid plexus hemosiderosis. Educational exhibit,

poster C1426.Vienna, Austria. European Congress of Radiology. doi: 10.1594/ecr2015/c-1426.
23. **Fisher C, Freiwald WA.** 2015. Whole-agent selectivity within the macaque face-processing system. Proc Natl Acad Sci USA **112:**14717–14722.
24. **Gavrieli Y, Sherman Y, Ben-Sasson SA.** 1992. Identification of programmed cell death in situ via specific labeling of nuclear DNA fragmentation. J Cell Biol **119:**493–501.
25. **Giknis MLA, Clifford CB**. 2006. Clinical laboratory parameters for Crl:CD (SD) rats. 1–14. Wilmington (MA): Charles River Laboratories.
26. **Grabill C, Silva AC, Smith SS, Koretsky AP, Rouault TA.** 2003. MRI detection of ferritin iron overload and associated neuronal pathology in iron regulatory protein-2 knockout mice. Brain Res **971:**95–106.
27. **Hinoda T, Fushimi Y, Okada T, Fujimoto K, Liu C, Yamamoto A, Okada T, Kido A, Togashi K.** 2015. Quantitative susceptibility mapping at 3 T and 1.5 T: evaluation of consistency and reproducibility. Invest Radiol **50:**522–530.
28. **Hope MD, Hope TA, Zhu C, Faraji F, Haraldsson H, Ordovas KG, Saloner D.** 2015. Vascular imaging with ferumoxytol as a contrast agent. AJR Am J Roentgenol **205:**W366–W373.
29. **Institute for Laboratory Animal Research.** 2011. Guide for the care and use of laboratory animals, 8th ed. Washington (DC): National Academies Press
30. **Jain TK, Reddy MK, Morales MA, Leslie-Pelecky DL, Labhasetwar V.** 2008. Biodistribution, clearance, and biocompatibility of iron oxide magnetic nanoparticles in rats. Mol Pharm **5:**316–327.
31. **Jenkinson M, Pechaud M, Smith S.** 2005**.** BET2: MR-based estimation of brain, skull and scalp surfaces. In: Eleventh annual meeting of the organization for human brain mapping, Toronto, 2005. Oxford (United Kingdom): Oxford Centre for Functional Magnetic Imaging of the Brain.
32. **Kim JS, Yoon TJ, Yu KN, Kim BG, Park SJ, Kim HW, Lee KH, Park SB, Lee JK, Cho MH.** 2005. Toxicity and tissue distribution of magnetic nanoparticles in mice. Toxicol Sci **89:**338–347.
33. **Kim SG, Harel N, Jin T, Kim T, Lee P, Zhao F.** 2013. Cerebral blood volume MRI with intravascular superparamagnetic iron oxide nanoparticles. NMR Biomed **26:**949–962.
34. **Kira R, Ohga S, Takada H, Gondo K, Mihara F, Hara T.** 2000. MR choroid plexus sign of iron overload. Neurology **55:**1340–1340.
35. **Klohs J, Deistung A, Ielacqua GD, Seuwen A, Kindler D, Schweser F, Vaas M, Kipar A, Reichenbach JR, Rudin M.** 2015. Quantitative assessment of microvasculopathy in arcAbeta mice with USPIO-enhanced gradient echo MRI. J Cereb Blood Flow Metab **36:**1614–1624.
36. **Kressler B, de Rochefort L, Liu T, Spincemaille P, Jiang Q, Wang Y.** 2010. Nonlinear regularization for per voxel estimation of magnetic susceptibility distributions from MRI field maps. IEEE Trans Med Imaging **29:**273–281.
37. **Kuhlpeter R, Dahnke H, Matuszewski L, Persigehl T, von Wallbrunn A, Allkemper T, Heindel WL, Schaeffter T, Bremer C.** 2007. R2 and R2* mapping for sensing cell-bound superparamagnetic nanoparticles: in vitro and murine in vivo testing. Radiology **245:**449–457.
38. **Kwon JT, Kim DS, Minai-Tehrani A, Hwang SK, Chang SH, Lee ES, Xu CX, Lim HT, Kim JE, Yoon BI, An GH, Lee KH, Lee JK, Cho MH.** 2009. Inhaled fluorescent magnetic nanoparticles induced extramedullary hematopoiesis in the spleen of mice. J Occup Health **51:**423–431.
39. **Lee MJ-E, Veiseh O, Bhattarai N, Sun C, Hansen SJ, Ditzler S, Knoblaugh S, Lee D, Ellenbogen R, Zhang M, Olson JM.** 2010. Rapid pharmacokinetic and biodistribution studies using chlorotoxin-conjugated iron oxide nanoparticles: a novel nonradioactive method. PLoS One **5:**1–8. Erratum: PLoS One **5:**1.
40. **Leite FP, Tsao D, Vanduffel W, Fize D, Sasaki Y, Wald LL, Dale AM, Kwong KK, Orban GA, Rosen BR, Tootell RB, Mandeville JB.** 2002. Repeated fMRI using iron oxide contrast agent in awake, behaving macaques at 3 Tesla. Neuroimage **16:**283–294.
41. **Levy M, Luciani N, Alloyeau D, Elgrabli D, Deveaux V, Pechoux C, Chat S, Wang G, Vats N, Gendron F, Factor C, Lotersztajn S, Luciani A, Wilhelm C, Gazeau F.** 2011. Long term in vivo biotransformation of iron oxide nanoparticles. Biomaterials **32:**3988–3999.
42. **Li J, Chang S, Liu T, Wang Q, Cui D, Chen X, Jin M, Wang B, Pei M, Wisnieff C, Spincemaille P, Zhang M, Wang Y.** 2012. Reducing the object orientation dependence of susceptibility effects in gradient echo MRI through quantitative susceptibility mapping. Magn Reson Med **68:**1563–1569.
43. **Li W, Tutton S, Vu AT, Pierchala L, Li BS, Lewis JM, Prasad PV, Edelman RR.** 2004. First-pass contrast-enhanced magnetic resonance angiography in humans using ferumoxytol, a novel ultrasmall superparamagnetic iron oxide (USPIO)-based blood pool agent. J Magn Reson Imaging **21:**46–52.
44. **Li W, Wu B, Liu C.** 2011. Quantitative susceptibility mapping of human brain reflects spatial variation in tissue composition. Neuroimage **55:**1645–1656.
45. **Lim IA, Faria AV, Li X, Hsu JT, Airan RD, Mori S, van Zijl PC.** 2013. Human brain atlas for automated region of interest selection in quantitative susceptibility mapping: application to determine iron content in deep gray matter structures. Neuroimage **82:**449–469.
46. **Liu C, Zhang N.** 2011. Nanoparticles in gene therapy: principles, prospects, and challenges, Chapter 13. p 509–562. In: Villaverde A, editor. Progress in molecular biology and translational science, vol 104, San Diego (CA): Elsevier.
47. **Liu J, Liu T, de Rochefort L, Ledoux J, Khalidov I, Chen W, Tsiouris AJ, Wisnieff C, Spincemaille P, Prince MR, Wang Y.** 2012. Morphology enabled dipole inversion for quantitative susceptibility mapping using structural consistency between the magnitude image and the susceptibility map. Neuroimage **59:**2560–2568.
48. **Liu T, Spincemaille P, de Rochefort L, Kressler B, Wang Y.** 2009. Calculation of susceptibility through multiple orientation sampling (COSMOS): a method for conditioning the inverse problem from measured magnetic field map to susceptibility source image in MRI. Magn Reson Med **61:**196–204.
49. **Liu T, Wisnieff C, Lou M, Chen W, Spincemaille P, Wang Y.** 2012. Nonlinear formulation of the magnetic field to source relationship for robust quantitative susceptibility mapping. Magn Reson Med **69:**467–476.
50. **Lu M, Cohen MH, Rieves D, Pazdur R.** 2010. FDA report: ferumoxytol for intravenous iron therapy in adult patients with chronic kidney disease. Am J Hematol **85:**315–319.
51. **Meeker RB, Williams K, Killebrew DA, Hudson LC.** 2012. Cell trafficking through the choroid plexus. Cell Adh Migr **6:**390–396.
52. **Moos T, Morgan EH.** 2004. The metabolism of neuronal iron and its pathogenic role in neurological disease: review. Ann N Y Acad Sci **1012:**14–26.
53. **Mounsey RB, Teismann P.** 2012. Chelators in the treatment of iron accumulation in Parkinson's disease. Int J Cell Biol **2012:**1–12.
54. **Muller RN, Gillis P, Moiny F, Roch A**. 1991. Transverse relaxivity of particulate MRI contrast media: from theories to experiments. Magn Reson Med **22:**178–182; discussion 195–196.
55. **Papp EA, Leergaard TB, Calabrese E, Johnson GA, Bjaalie JG.** 2014. Waxholm space atlas of the Sprague Dawley rat brain. Neuroimage **97:**374–386. Erratum: Neuroimage **105:**561–562.
56. **Pei M, Nguyen TD, Thimmappa ND, Salustri C, Dong F, Cooper MA, Li J, Prince MR, Wang Y.** 2014. Algorithm for fast monoexponential fitting based on auto-regression on linear operations (ARLO) of data. Magn Reson Med **73:**843–850.
57. **Petters C, Irrsack E, Koch M, Dringen R.** 2014. Uptake and metabolism of iron oxide nanoparticles in brain cells. Neurochem Res **39:**1648–1660.
58. **Poplawsky AJ, Kim SG.** 2014. Layer-dependent BOLD and CBV-weighted fMRI responses in the rat olfactory bulb. Neuroimage **91:**237–251.
59. **Qiu D, Zaharchuk G, Christen T, Ni WW, Moseley ME.** 2012. Contrast-enhanced functional blood volume imaging (CE-fBVI): enhanced sensitivity for brain activation in humans using the ultrasmall superparamagnetic iron oxide agent ferumoxytol. Neuroimage **62:**1726–1731.
60. **Redzic ZB, Preston JE, Duncan JA, Chodobski A, Szmydynger-Chodobska J.** 2005. The choroid plexus–cerebrospinal fluid system: from development to aging. Curr Top Dev Biol **71:**1–52.

61. **Roemer PB, Edelstein WA, Hayes CE, Souza SP, Mueller OM.** 1990. The NMR phased array. Magn Reson Med **16:**192–225.
62. **Rouault TA, Zhang DL, Jeong SY.** 2009. Brain iron homeostasis, the choroid plexus, and localization of iron transport proteins. Metab Brain Dis **24:**673–684.
63. **Schwiedrzik CM, Zarco W, Everling S, Freiwald WA.** 2015. Face patch resting state networks link face processing to social cognition. PLoS Biol **13:**1–27.
64. **Shmueli K, de Zwart JA, van Gelderen P, Li TQ, Dodd SJ, Duyn JH.** 2009. Magnetic susceptibility mapping of brain tissue in vivo using MRI phase data. Magn Reson Med **62:**1510–1522.
65. **Simon GH, von Vopelius-Feldt J, Fu Y, Schlegel J, Pinotek G, Wendland MF, Chen MH, Daldrup-Link HE.** 2006. Ultrasmall supraparamagnetic iron oxide-enhanced magnetic resonance imaging of antigen-induced arthritis: a comparative study between SHU 555 C, ferumoxtran 10, and ferumoxytol. Invest Radiol **41:**45–51.
66. **Singh N, Jenkins GJ, Asadi R, Doak SH.** 2010. Potential toxicity of superparamagnetic iron oxide nanoparticles (SPION). Nano Rev **1:**1–15. doi:10.3402/nano.v1i0.5358
67. **Sossa DE, Chiang F, Verde AR, Sossa DG, Castillo M.** 2013. Transfusional iron overload presenting as choroid plexus hemosiderosis. JBR-BTR **96:**391.
68. **Sun C, Lee JS, Zhang M.** 2008. Magnetic nanoparticles in MR imaging and drug delivery. Adv Drug Deliv Rev **60:**1252–1265.
69. **Tang TY, Muller KH, Graves MJ, Li ZY, Walsh SR, Young V, Sadat U, Howarth SP, Gillard JH.** 2009. Iron oxide particles for atheroma imaging. Arterioscler Thromb Vasc Biol **29:**1001–1008.
70. **Varallyay CG, Nesbit E, Fu R, Gahramanov S, Moloney B, Earl E, Muldoon LL, Li X, Rooney WD, Neuwelt EA.** 2013. High-resolution steady-state cerebral blood volume maps in patients with central nervous system neoplasms using ferumoxytol, a superparamagnetic iron oxide nanoparticle. J Cereb Blood Flow Metab **33:**780–786.
71. **Wang Y**. 2013. Quantitative susceptibility mapping: magnetic resonance imaging of tissue magnetism, p. 95. New York (NY): CreateSpace Independent Publishing Platform.
72. **Wang Y, Liu T.** 2014. Quantitative susceptibility mapping (QSM): decoding MRI data for a tissue magnetic biomarker. Magn Reson Med **73:**82–101.
73. **Wharton S, Schäfer A, Bowtell R.** 2010. Susceptibility mapping in the human brain using threshold-based k-space division. Magn Reson Med **63:**1292–1304.
74. **Yang HW, Hua MY, Liu HL, Huang CY, Tsai RY, Lu YJ, Chen JY, Tang HJ, Hsien HY, Chang YS, Yen TC, Chen PY, Wei KC.** 2011. Self-protecting core–shell magnetic nanoparticles for targeted, traceable, long half-life delivery of BCNU to gliomas. Biomaterials **32:**6523–6532.
75. **Yang M, Christoforidis GA, Figueredo T, Heverhagen JT, Abduljalil A, Knopp MV.** 2005. Dosage determination of ultrasmall particles of iron oxide for the delineation of microvasculature in the Wistar rat brain. Invest Radiol **40:**655–660.
76. **Yokel RA, Crossgrove JS, Bukaveckas BL.** 2003. Manganese distribution across the blood-brain barrier. II. Manganese efflux from the brain does not appear to be carrier mediated. Neurotoxicology **24:**15–22.